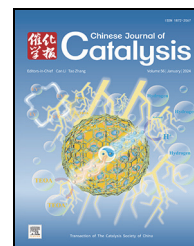


available at www.sciencedirect.comjournal homepage: www.sciencedirect.com/journal/chinese-journal-of-catalysis

Article

Uleashing efficient and CO-resilient alkaline hydrogen oxidation of Pd₃P through phosphorus vacancy defect engineering



Yuting Yang^{a,b,1}, Luyan Shi^{a,1}, Qinrui Liang^a, Yi Liu^a, Jiaxin Dong^a, Tayirjan Taylor Isimjan^{d,*}, Bao Wang^c, Xiulin Yang^{a,*}

^a Guangxi Key Laboratory of Low Carbon Energy Materials, School of Chemistry and Pharmaceutical Sciences, Guangxi Normal University, Guilin 541004, Guangxi, China

^b School of Environmental Science and Engineering, Sun Yat-sen University, Guangzhou 510275, Guangdong, China

^c State Key Laboratory of Biochemical Engineering, Institute of Process Engineering, Chinese Academy of Sciences, Beijing 100190, China

^d Saudi Arabia Basic Industries Corporation (SABIC) at King Abdullah University of Science and Technology (KAUST), Thuwal 23955-6900, Saudi Arabia

ARTICLE INFO

Article history:

Received 11 September 2023

Accepted 7 November 2023

Available online 10 January 2024

Keywords:

Hydrogen oxidation reaction

CO tolerance

Phosphorus vacancy

V_p-Pd₃P@C

Bowl-like hemisphere

ABSTRACT

A high-performance and highly CO-resilient hydrogen oxidation reaction (HOR) electrocatalyst is heralded as core material to solve the commercial deployment of hydrogen fuel cells. Phosphorus vacancies, as a type of delicate point defect, could effectively and flexibly modulate the catalytic performance. Therefore, based on the vacancy design philosophy of “less is more”, we synthesize a phosphorus-vacancy-rich Pd₃P@C (V_p-Pd₃P@C) catalyst with bowl-like hemisphere structure for alkaline HOR, for the first time. The V_p-Pd₃P@C catalyst exhibits remarkable mass activity and exchange current density of 1.66 mA μg_{Pd}⁻¹ and 3.2 mA cm⁻², respectively, surpassing those of Pd₃P@C (0.45 mA μg_{Pd}⁻¹, 1.78 mA cm⁻²) and commercial Pt/C (0.3 mA μg_{Pt}⁻¹, 2.29 mA cm⁻²). Intriguingly, the catalyst can tolerate 1000 ppm CO that Pt/C catalyst lacks. Density functional theory calculations uncover that the optimal local coordination environment and favorable electronic structure that rooted from phosphorus vacancy enable optimum adsorption kinetics of hydrogen and hydroxyl while concomitantly suppressing Pd 4d → CO 2π* back donation, contributing to the remarkable HOR reactivity and CO tolerance.

© 2024, Dalian Institute of Chemical Physics, Chinese Academy of Sciences.

Published by Elsevier B.V. All rights reserved.

1. Introduction

Alkaline anion exchange membrane fuel cells (AEMFCs) facilitate the direct conversion of hydrogen's chemical energy into electricity, serving as the cornerstone devices in burgeoning green hydrogen economies [1]. While AEMFCs offer the potential to employ nonprecious metal catalysts for the sluggish cathodic oxygen reduction reaction (ORR), there are nu-

merous unresolved challenges to establishing AEMFCs as vibrant and competitive entities [2]. The primary concern revolves around the development of a cost-effective and efficient catalyst for the anodic HOR. To date, the Pt/C catalyst stands as the benchmark HOR electrocatalyst [3], however, its surface is susceptible to poisoning by even trace amounts of CO present in the hydrogen feed — a mere 1 ppm of CO can incapacitate approximately 90% of Pt's active sites. As a CO molecule nears

* Corresponding author. E-mail: xlyang@gxnu.edu.cn (X. Yang), isimjant@sabic.com (T. T. Isimjan).

¹ Contributed equally to this work.

This work was supported by the National Natural Science Foundation of China (52363028, 21965005), the Natural Science Foundation of Guangxi Province (2021GXNSFAA076001), the Innovation and entrepreneurship training for college students (202210602045), the Innovation Project of Guangxi Graduate Education (YCSW2023140), and the Guangxi Technology Base and Talent Subject (GUIKE AD20297039).

[https://doi.org/10.1016/S1872-2067\(23\)64570-X](https://doi.org/10.1016/S1872-2067(23)64570-X)

the Pt surface, its $5s$ and $2\pi^*$ orbitals undergo broadening and downward shift. The $5s$ orbital will be split into a bonding and anti-bonding orbital [4]. It has been reported that CO–Pt bonding arises from the transfer of electron from the $5s$ orbitals of CO to the Pt d -orbitals ($\text{CO } 5s \rightarrow \text{Pt } 5d$), and the concurrent back-donation of electron from the Pt d -orbitals to CO $2\pi^*$ orbitals [5]. Therefore, the interaction between the CO $2\pi^*$ orbitals and the d states of Pt dictates the CO adsorption energy on the Pt surface. As a direct implication, AEMFCs necessitate the use of the more expensive high-purity hydrogen ($\approx \$4.2 \text{ kg}^{-1}$), sidelining the economical option of crude H_2 derived from steam reforming ($\approx \$1.5 \text{ kg}^{-1}$) [5,6]. Furthermore, the sluggish HOR/HER kinetics on Pt/C catalyst in alkaline electrolytes generally exhibits 2–3 orders of magnitude lower than in acidic media [7]. If CO-contaminated H_2 fuels are fed, the power and longevity of AEMFCs were deeply hampered by catalyst poisoning and sluggish kinetics. Hence, it is eminently imperative but challenging to explore electrocatalysts with unfavorable chemisorption of CO and high HOR catalytic performance. Moreover, a profound grasp of alkaline HOR mechanisms can significantly steer catalyst design and performance refinement.

The anode of AEMFCs facilitates the process of HOR by oxidizing hydrogen to water. This procedure is governed by either the Tafel-Volmer or Heyrovsky-Volmer sequence. In this sequence, H_2 molecules are adsorbed onto active sites and dissociated to form adsorbed hydrogen (H_{ads}). This H_{ads} subsequently react with OH^- ions or adsorbed hydroxyl (OH_{ads}) to produce H_2O [6]. The Hydrogen Binding Energy (HBE) theory accentuates the role of H_{ads} as a pivotal intermediate in alkaline HOR activity [8,9]. But, as pH rises and the proton donor shifts from H_3O^+ to H_2O , coupled with hydroxyl species in alkaline environments, the Volmer step ($\text{H}_{\text{ads}} + \text{OH}_{\text{ads}} \rightarrow \text{H}_2\text{O} + 2^* \text{ sites}$) becomes the rate-determining step (RDS) [10,11]. Consequently, a bifunctional mechanism arises, striving to harmonize the ideal HBE and OHBE, thereby guiding the conception of optimal alkaline HOR electrocatalysts, such as IrMo alloy, BCC-phased PdCu alloy, Ru/Ni-NiO@C, $\text{Pt}_6\text{NCs/C}$, among others [10,12–14]. Additionally, extensive efforts have been made to mitigate the threats of CO poisoning on Pt-based catalysts [15,16]. For instance, Luo *et al.* [17] have conducted groundbreaking research on the fabrication of intermetallic $\text{Ru}_3\text{Sn}_7/\text{C}$ featuring more vacant d -orbitals, thus reducing the back-donation process from metal d -orbitals into the CO $2\pi^*$ orbitals, ultimately weakening the Ru–CO bond strength and enhancing CO tolerance. However, despite significant efforts, only a few electrocatalysts have demonstrated robust performance under high CO levels ($> 100 \text{ ppm}$).

Palladium (Pd) exhibits similar optimal hydrogen binding strength to Pt but possesses more abundant reserves, exceptional stability, and higher CO tolerance, making it a potential candidate for HOR to achieve the aforementioned goals [18,19]. To further enhance the performance of Pd-based catalysts, extensive research efforts have focused on optimizing their composition and electronic structure [20]. Despite notable achievements, the operating performance of these catalysts still lags behind the requirements for commercial deployment. Recently, transition-metal phosphides (TMPs) have garnered

attention in the catalytic field due to their functional diversity and high catalytic activity [21,22]. However, Pd-based phosphides are poorly reported in the press thus far owing to their complicated preparation and harsh synthesis conditions [23]. Concurrently, innovating open nanostructures, like bowl-like hemispheres, has showcased its prowess in magnifying the electrocatalytic traits of TMPs. These structures foster efficient reactant mass transfer across both outer and inner facets, revealing more active sites [24]. Beyond morphological enhancements, the introduction of vacancies, especially phosphorus vacancy, emerges as a potent tool for refining the electrocatalytic competencies of phosphides by modulating their electronic structures, reshaping their adsorption behaviors, and subsequently fortifying both their activity and robustness [25]. However, investigations into introducing phosphorus vacancy in TMPs and evaluating their impact on HOR performance are still in their infancy and require in-depth exploration.

Herein, we create phosphorus vacancy in palladium phosphides anchored on hollow bowl-like carbon hemispheres through a thermal annealing process and extensively investigate their performance in alkaline HOR electrocatalysis from the perspective of phosphorus vacancy concentration. Benefiting from the open structures and abundant phosphorus vacancies, the optimized $\text{V}_p\text{-Pd}_3\text{P@C}$ catalyst exhibits a potentially transformative combination of high activity and excellent durability, along with remarkable CO tolerance. DFT calculations suggest that the electronic interaction between Pd and P atoms, along with the plentiful phosphorus vacancies, optimize the adsorption of both hydrogen and hydroxyl species. Furthermore, we simulate the alkaline HOR reaction pathways, revealing that by increasing phosphorus vacancy concentration in Pd_3P , the RDS can be effectively shifted from the desorption of adsorbed H_2O to the formation of H_2O , thereby substantially enhancing the intrinsic HOR activity through promotion of the Volmer step.

2. Experimental

2.1. Materials

Tetraethyl silicate (TEOS, $\geq 28.0\%$, Aladdin, 500 mL), formaldehyde solution (HCHO, 37.0%–40.0%, Xilong Science, 500 mL), ammonia aqueous ($\text{NH}_3 \cdot \text{H}_2\text{O}$, 25.0%–28.0% Xilong Science, 500 mL), Pluronic F127 ($\text{PEO}_{100}\text{PPO}_{65}\text{PEO}_{100}$, Aladdin, 1 kg), sodium hypophosphite monohydrate ($\text{NaH}_2\text{PO}_2 \cdot \text{H}_2\text{O}$, $\geq 99\%$, Xilong Science, 500 g), potassium tetrachloropalladate (K_2PdCl_4 , $> 98\%$, Aladdin, 5 g), potassium hydroxide (KOH, AR, $> 90\%$, Macklin, 500 g), ethanol (AR, 99.5%, Xilong Science, 500 mL), commercial Pt/C (20 wt% Pt, Alfa Aesar, 1 g), commercial Ru/C (5 wt% Ru, Macklin, 5 g), Nafion solution (5 wt%, Alfa Aesar, 100 mL), deionized water ($18.25 \text{ M}\Omega \text{ cm}^{-1}$). All chemicals were analytical grade and could be used directly as received.

2.2. Synthesis of bowl-like hollow carbon spheres (BHCS)

The BHCS were prepared based on previous reports with a slightly modification. Typically, tetraethyl orthosilicate (TEOS, 3.5 mL), resorcinol (0.4 g) and formaldehyde (0.56 mL) were added to the solution containing 70 mL of ethanol, 10 mL of H₂O, and 3 mL of ammonia solution (28 wt%). After stirring well on a magnetic stirrer for 6 h at room temperature, 1.5 mL of TEOS was added to the mixture and continued stirring for 24 h. The obtained flesh pink precipitates were centrifuged, washed with water and ethanol in sequence, and dried at 60 °C. The precipitates were further carbonized under an N₂ atmosphere at 700 °C (2 °C min⁻¹) for 5 h. Finally, the BHCS with a novel semiconcave geometry could be easily produced by removing silica templates with 3 mol L⁻¹ KOH solution at 70 °C.

2.3. Synthesis of V_p-Pd₃P@C

80 mg BHCS were ultrasonically dispersed into 10 mL of H₂O containing 80 mg F127, and 10 mg K₂PdCl₄ followed by stirring and ultrasound for 1 h. The precursor was collected by centrifugation, washed with water and ethanol for several times and dried at 60 °C. Then, the precursor and NaH₂PO₂·H₂O with a mass ratio of 1:3 were placed in a tube furnace, and heated up to 350 °C for 2 h with a heating rate of 2 °C min⁻¹ in N₂ atmosphere to obtain V_p-Pd₃P@C. Following the same line of thought, we obtained other palladium phosphide nanoparticles, which were labeled as Pd/Pd₃P@C, Pd_{3.20}P₁₂@C, Pd₃P@C and Pd₅P₂@C in turn of the temperature (250, 450 °C) and Pd/P mass ratio (1:2, 1:4) from lowest to highest. In addition, we synthesized Pd@C for comparison without phosphating treatment.

2.4. Materials characterization

The crystal structure was characterized by powder X-ray diffraction (XRD) using a Rigaku D/Max with Cu K_α (λ = 1.540598 Å) radiation. Electron paramagnetic resonance (EPR) spectra were measured by Bruker E500 spectrometer. Scanning electron microscope (SEM) measurements were performed on FEI Quanta 200 system. Transmission electron microscopy (TEM) images were recorded on a JEM-2100F electron microscope equipped with an energy dispersive X-ray detector (EDX) at an acceleration voltage of 200 kV. X-ray photoelectron spectroscopy (XPS) was conducted on Thermo Fisher EscaLab 250XI spectrometer equipped with an Al K_α X-ray source. Ultraviolet photoelectron spectroscopy (UPS) was performed on X-ray photoelectron spectroscopy (PHI5000 VersaProbe III). Raman spectra were taken on a Raman microscope (Renishaw®) excited with a 514 nm excitation laser. Zeta-potential measurements were carried out on Malvern Zetasizer Nano ZSP. Inductively coupled plasma atomic emission spectroscopy (ICP-AES) was taken on Intrepid II XSP instrument.

2.5. Computational methods

Spin-polarized density functional theory (DFT) calculations were performed using the Vienna ab initio simulation package

(VASP) [26,27]. The generalized gradient approximation proposed by Perdew, Burke, and Ernzerhof (GGA-PBE) is selected for the exchange-correlation potential [28]. The pseudo-potential was described by the projector-augmented-wave (PAW) method [29]. The geometry optimization is performed until the Hellmann-Feynman force on each atom is smaller than 0.03 eV Å⁻¹. The energy criterion is set to 10⁻⁶ eV in iterative solution of the Kohn-Sham equation. The Kohn-Sham valence electronic wavefunction was expanded in a plane-wave basis set with a cutoff at 400 eV. Adsorption energy was calculated according to $E_{\text{adsorption}} = E_{\text{total}} - E_{\text{substrate}} - E_{\text{adsorbate}}$.

3. Results and discussion

3.1. Synthesis and structural characterization

Fig. 1(a) depicts the synthetic process for V_p-Pd₃P@C, which involves a sol-gel approach and phosphating strategy. The process begins with the formation of monodispersed silica spheres through the hydrolysis and condensation of TEOS. Resorcinol-formaldehyde (RF) oligomers then condense onto the SiO₂ cores *via* heterogeneous nucleation. To achieve the bowl-like structure, TEOS is introduced for the second time at a specific time point, leading to the formation of highly uniform silica particles on the RF shell through a subsequent heterogeneous-nucleation process. The residual RF oligomers and silica particles are co-condensed to form a composite RF/silica layer [24]. After carbonization and desilication, HBCH are obtained. The bowl-like V_p-Pd₃P@C with enriched phosphorus vacancy is subsequently synthesized through a phosphating process using NaH₂PO₂·H₂O as a phosphorus source. Obvious crystal imperfections like phosphorus vacancy are evidenced in V_p-Pd₃P@C, which can be attributed to the temporary high pressure during the thermal decomposition process, resulting from the considerable amounts of PH₃ gas due to the excess of P source [25]. Later, in the same vein, we precisely regulated the phosphating degree of the Pd precursor by adjusting the decomposition rate of NaH₂PO₂·H₂O based on temperature (250, 450 °C) and Pd/P mass ratio (1:2, 1:4) control, and achieved a series of palladium phosphide (Pd_xP_y@C) with different crystalline phases, namely Pd/Pd₃P@C, Pd_{3.20}P₁₂@C, Pd₃P@C and Pd₅P₂@C, respectively (See experimental methods for details).

The morphological evolution of HBCH and V_p-Pd₃P@C is examined using SEM. As depicted in Fig. 1(b), SiO₂/SiO₂/RF exhibits a monodispersed spherical morphology. After carbonization and alkali-steeping, the initial spherical shape evolves into invaginated spheres, consequently yielding a concave bowl-shaped structure (Fig. 1(c)). Importantly, V_p-Pd₃P@C retains the distinctive bowl-like morphology (Fig. 1(d)). The bowl-like structure offers advantages over intact spheres in terms of eliminating inert bulk interiors and shortening the transport distance of reactants [30,31]. TEM confirms the hollow bowl-like nature of V_p-Pd₃P@C (Fig. 1(e)). High-resolution TEM (HRTEM) analysis reveals lattice streak spacing of 0.224 and 0.23 nm, corresponding to the (031) and (220) crystal facets of V_p-Pd₃P@C, respectively (Fig. 1(f)). Additionally, the relative Fast Fourier Transform (FFT) image demonstrates the

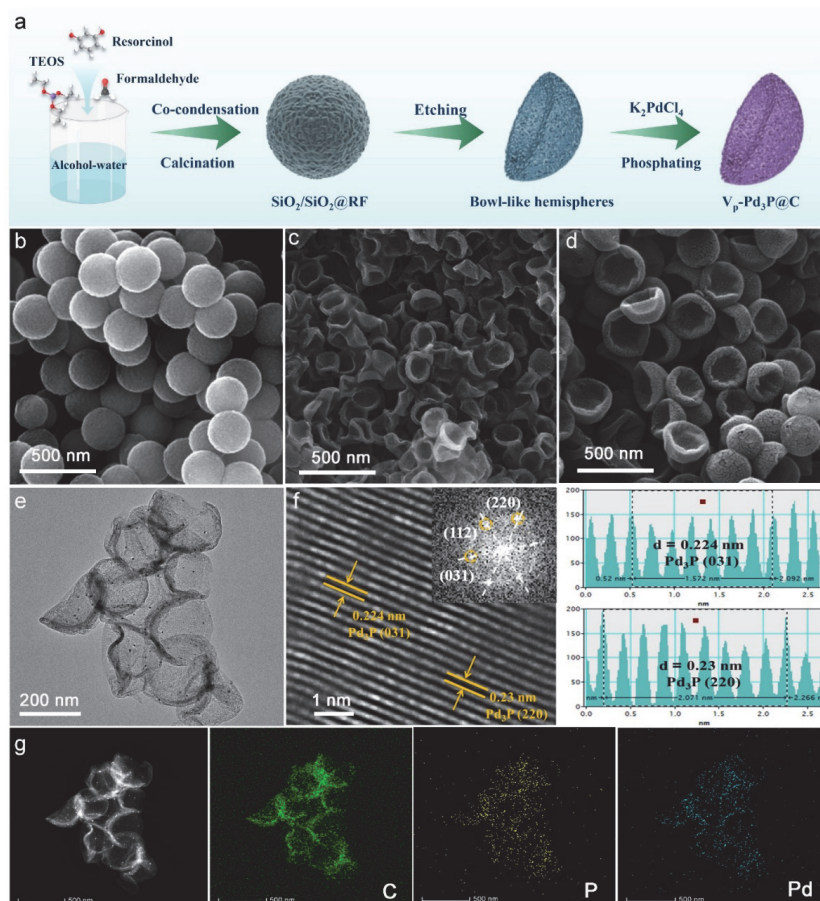


Fig. 1. (a) Schematic protocol of the synthesis strategy for $V_p\text{-Pd}_3\text{P@C}$. SEM images of $\text{SiO}_2/\text{SiO}_2\text{@RF}$ (b), bowl-like hemispheres (c) and $V_p\text{-Pd}_3\text{P@C}$ (d). TEM (e) and HRTEM (f) images of the $V_p\text{-Pd}_3\text{P@C}$ (inset: the corresponding FFT pattern). (g) HAADF-STEM image and corresponding elemental mappings of $V_p\text{-Pd}_3\text{P@C}$.

well-resolved and continuous crystal lattice of Pd_3P (Fig. 1(f) illustration). Elemental mapping analysis further confirms the uniform distribution of C, P, and Pd elements throughout the structure (Fig. 1(g)).

Palladium phosphides exhibit various crystal structures depending on the specific metal-phosphorus coordination form. To investigate the crystal structure changes in $\text{Pd}_x\text{P}_y\text{@C}$ samples, we performed an XRD analysis. Figs. 2(a) and (b) demonstrates the successful synthesis of pure phase Pd@C , $V_p\text{-Pd}_3\text{P@C}$, $\text{Pd}_{3.20}\text{P}_{12}\text{@C}$, $\text{Pd}_3\text{P@C}$ and $\text{Pd}_5\text{P}_2\text{@C}$, with all XRD peaks of the $\text{Pd}_x\text{P}_y\text{@C}$ samples matching well with the Pd@C (PDF#05-0681, PDF#01-1310), Pd_3P (PDF#01-089-3046), $\text{Pd}_{3.20}\text{P}_{12}$ (PDF#42-0922), and Pd_5P_2 (PDF#19-0887) cards. While multiphase components are observed in $\text{Pd/Pd}_3\text{P@C}$, the XRD pattern predominantly indicates the presence of metallic Pd. This observation suggests that the lower temperature (250 °C) used during phosphating is insufficient for the full decomposition of $\text{NaH}_2\text{PO}_2\cdot\text{H}_2\text{O}$. Fig. 2(c) illustrates the variation in crystallographic structures of palladium phosphide as a function of phosphating temperature and Pd/P mass ratio. To qualitatively confirm the existence of phosphorus vacancy in these samples, EPR measurements were conducted (Fig. 2(d)). Notably, sharp peaks at $g = 2.002$ are observed in the EPR spectra of $\text{Pd}_x\text{P}_y\text{@C}$, indicating the presence of phosphorus vacancy cap-

turing unpaired electrons. This is distinctly different from the case of Pd@C [32]. Interestingly, the relative content of phosphorus vacancy can be effectively regulated by adjusting the phosphating temperature and Pd/P mass ratio, providing one path for optimization. The EPR signal for $V_p\text{-Pd}_3\text{P@C}$, annealed at 350 °C with a Pd/P mass ratio of 1:3, is notably more intense, suggesting a greater concentration of phosphorus vacancies. The presence of rich phosphorus vacancy and related unpaired electrons in $V_p\text{-Pd}_3\text{P@C}$ not only affect the local electronic structure and orbital coupling, but also expose more active sites that can modify the adsorption ability of reactive intermediates [32,33]. The defects within the carbon support can also affect the performance of electrocatalysts [34]. We then performed the Raman spectroscopy to achieve information pertaining to the structural defects of samples. The Raman spectroscopy results (Fig. S1) reveal that the intensity ratio (I_D/I_G) between the D-band ($\approx 1362\text{ cm}^{-1}$, disordered defective C-sp^3) and G-band ($\approx 1587\text{ cm}^{-1}$, ordered graphitic C-sp^2) for the HBCH support is close to 1.80, indicating enrichment of structural defects in the carbon support [35]. The I_D/I_G of $\text{Pd}_x\text{P}_y\text{@C}$ is somewhat attenuated, likely due to the partial occupation of carbon defect sites by Pd_xP_y species. This indicates that HBCH can serve as protective shells, contributing to the prevention of coalescence, peeling off and dissolution of Pd_xP_y nanoparticles

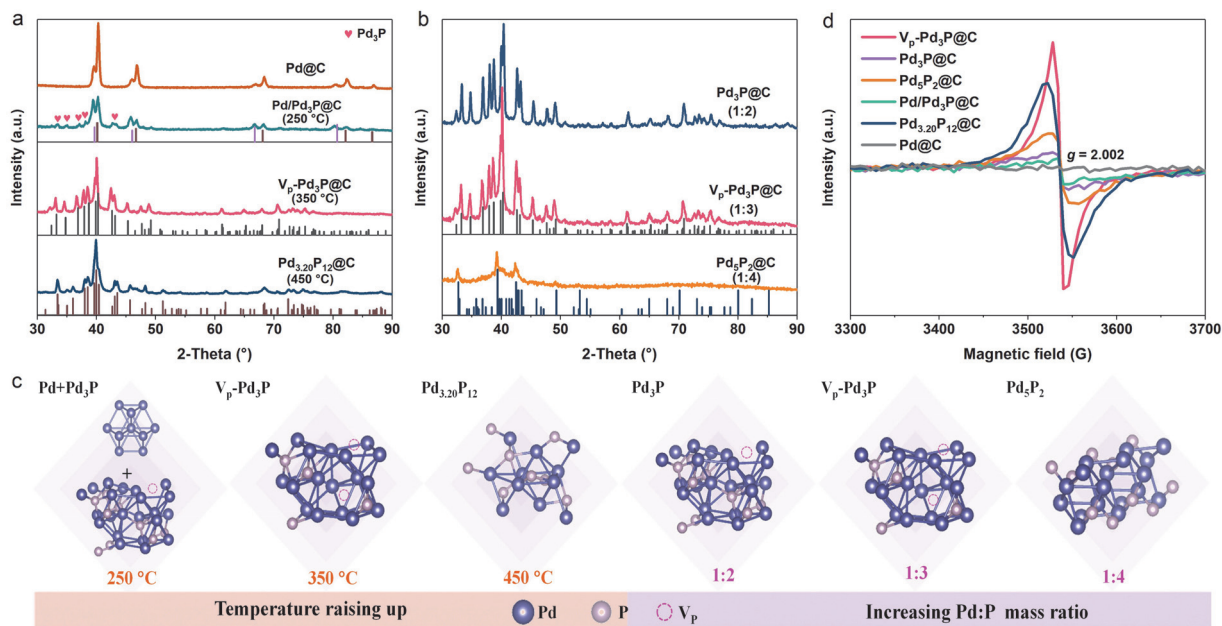


Fig. 2. (a,b) Powder XRD patterns of synthesized palladium phosphides ($\text{Pd}_x\text{P}_y@C$). (c) Crystal structures of various palladium phosphides spanning a range of temperature and Pd:P mass ratios. (d) EPR spectra of $\text{Pd}_x\text{P}_y@C$.

during the electrochemical measurements and ensuring long-term stability [13,36,37].

The depth profile XPS provide valuable chemical and structural information about the samples. The C 1s peak is calibrated at 284.0 eV as a standard reference (Fig. S2). In the high-resolution Pd 3d spectrum (Fig. 3(a)), the deconvoluted peaks at 335.2 and 340.5 eV correspond to bulk metallic palladium (Pd^0), while the peaks center at 337.6 and 342.8 eV account for electro-depleted palladium species ($\text{Pd}^{\delta+}$). In $\text{V}_p\text{-Pd}_3\text{P}@C$, the Pd^0 peak shows a positive shift of 0.55 eV compared to pure $\text{Pd}@C$, indicating electron transfers from Pd to P, resulting in positively charged $\text{Pd}^{\delta+}$ and negatively charged $\text{P}^{\delta-}$ [38]. This phenomenon arises from the hybridization of *d-p* orbitals through the introduction of *p*-block P species [17]. Moreover, The Pd^0 peak in $\text{V}_p\text{-Pd}_3\text{P}@C$ displays a larger positive shift in binding energy relative to other $\text{Pd}_x\text{P}_y@C$ samples, illustrating stronger electron interaction between Pd and P due to the increased *d-p* orbital hybridization resulting from the presence of more phosphorus vacancies (Fig. 3(b)). Additionally, the different proportion of $\text{Pd}^{\delta+}$ in $\text{Pd}_x\text{P}_y@C$ samples result from their differential sensitivity to air, leading to varying degrees of oxidation (Fig. 3(d)). Pertaining to the P 2p core level spectra (Fig. 3(c)), the prominent peak at 133.9 eV represents the P–O bond, likely a result of extended exposure to air [37]. The signal at a binding energy of 133.1 eV is attributed to the P–C bond, suggesting the doping of P into carbon support [37]. Another weak peak observed at about 129.8 eV is associated with the Pd–P bond, indicating the formation of palladium phosphide [39]. The presence of phosphorus vacancy in $\text{Pd}_x\text{P}_y@C$ samples can be confirmed by XPS through the analysis of the proportion of fitting peaks as well as the modified electronic structure of P atoms. By measuring the signals from the P 2p spectra, the P percentage (present as Pd–P bond) in

$\text{V}_p\text{-Pd}_3\text{P}@C$ is calculated to be 20.7%, which is lower than that in other $\text{Pd}_x\text{P}_y@C$ samples (Fig. 3(d)). This decrease in Pd-P content is associated with the formation of a P-poor phase and the presence of phosphorus vacancies [25,40]. Therefore, noticeable electronic differences exist among these crystal structures.

3.2. Electrocatalytic performance

The electrocatalytic properties of the catalysts were evaluated using the rotating disk electrode (RDE) technique in H_2 -saturated 0.1 mol L^{-1} KOH electrolyte. Through systematic experiments contingent on temperature and Pd/P mass ratio, we concluded that peak HOR activity is achieved on $\text{V}_p\text{-Pd}_3\text{P}@C$ with the optimal phosphorous vacancy, annealed at 350 °C and a Pd/P mass ratio of 1:3. Fig. S3(a) shows the polarization curves of the catalysts in H_2 -saturated electrolyte, the anode current density of $\text{V}_p\text{-Pd}_3\text{P}@C$ increases sharply with increasing potential, which stands out as the best catalyst of the series, revealing that the appropriate phosphating temperature and Pd/P mass ratio are critical for successful Pd utilization. Tafel plots in Fig. S3(b) also demonstrate the fastest HOR kinetics on $\text{V}_p\text{-Pd}_3\text{P}@C$. We further extracts the exchange current densities (j_0) of the as-prepared catalysts from the linear fitting of micropolarization regions (–5 to 5 mV, Fig. S3(c)) through the simplified Butler-Volmer equation [41]. The j_0 of $\text{Pd}_x\text{P}_y@C$ samples are found to be strongly related to the Pd-P content, with the top performing sample ($\text{V}_p\text{-Pd}_3\text{P}@C$) at the summit with a Pd-P content of 20.7%, neither too high nor too low (Fig. S3(d)). Thus, we selected $\text{V}_p\text{-Pd}_3\text{P}@C$ for the subsequent catalytic study.

We qualitatively evaluated the HOR activities of $\text{V}_p\text{-Pd}_3\text{P}@C$, $\text{Pd}_3\text{P}@C$, $\text{Pd}@C$, commercial Pd/C and commercial Pt/C in

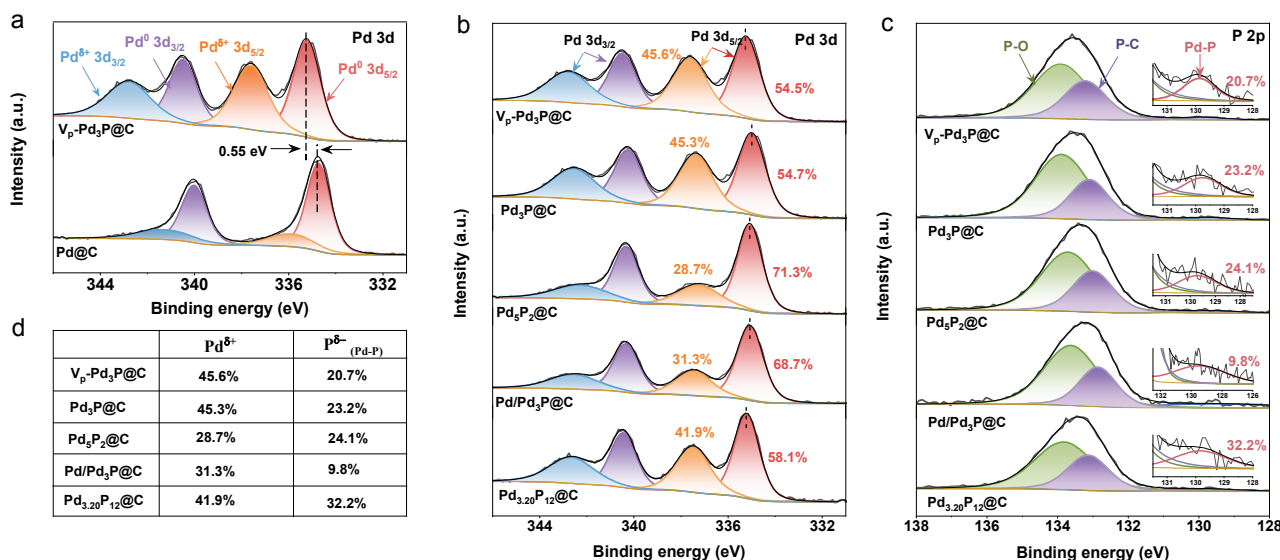


Fig. 3. High-resolution XPS spectra of Pd 3d (a, b), and P 2p (c) spectra of regions in $\text{Pd}_x\text{P}_y\text@C$. (d) $\text{Pd}^{\delta+}$ and $\text{Pd}^{\delta-}$ percentages in $\text{Pd}_x\text{P}_y\text@C$.

H_2 -saturated 0.1 mol L^{-1} KOH electrolyte by comparing the current responses. The HOR polarization curves in Fig. 4(a), it is apparent that $V_p\text{-Pd}_3\text{P@C}$ possesses the highest anodic current density from the kinetic to the diffusion-limiting regions, outperforming the $\text{Pd}_3\text{P@C}$ with lower concentration phosphorus vacancy and other references. A Control experiment conducted in N_2 -saturated electrolyte exhibits negligible anodic current, confirming that the anodic current primarily arises from H_2 oxidation (Fig. S4). Furthermore, we tested the polarization curves of $V_p\text{-Pd}_3\text{P@C}$ as a function of the rotating speed, where the limiting current density grows with the elevation of rotation rate, corroborating a H_2 mass-transport controlled process (Fig. 4(b)). The Koutecky-Levich plot constructed at 75 mV (inset of Fig. 4(b)) exhibits a linear relationship between the inverse of the overall current density and the square root of the rotation rate, yielding a calculated slope of $5.16 \text{ cm}^2 \text{ mA}^{-1} \text{ s}^{-1/2}$, which is close to the theoretical value ($4.87 \text{ cm}^2 \text{ mA}^{-1} \text{ s}^{-1/2}$) for the two-electron transfer HOR process [42]. To further investigate the HOR catalytic mechanism, Tafel slopes were obtained by plotting the kinetic current density (j_k) against overpotential for the prepared catalysts. The asymmetric behavior of Tafel plot indicates that $V_p\text{-Pd}_3\text{P@C}$ follows the Heyrovsky-Volmer mechanism, with the Volmer step being the RDS (Fig. 4(c)) [43]. As plotted in Fig. 4(d), the j_0 of samples are obtained from micro-polarization region (-5 to 5 mV). The j_0 of $V_p\text{-Pd}_3\text{P@C}$ (3.2 mA cm^{-2}) surpasses those of $\text{Pd}_3\text{P@C}$ (1.79 mA cm^{-2}), Pd@C (0.72 mA cm^{-2}), commercial Pd/C (1.09 mA cm^{-2}), and commercial Pt/C (2.25 mA cm^{-2}) catalyst, implying good inherent HOR activity of $V_p\text{-Pd}_3\text{P@C}$ (Fig. 4(e)). Additionally, the j_k value is calculated from Koutecky-Levich equation at 50 mV. $V_p\text{-Pd}_3\text{P@C}$ possesses a geometric j_k of 51.19 mA cm^{-2} , representing 3.0-, 16.5-, 13.7- and 4.2-fold increases compared with $\text{Pd}_3\text{P@C}$ (16.96 mA cm^{-2}), Pd@C (3.10 mA cm^{-2}), commercial Pd/C (3.75 mA cm^{-2}) and commercial Pt/C (12.27 mA cm^{-2}), respectively. Furthermore, the j_k values are normalized by the respective mass of platinum group metals (PGM) to yield mass activity (MA) at 50 mV, providing a more accurate picture

of HOR activity. Meanwhile, the PGM contents were determined by ICP-AES measurements (Table S1). $V_p\text{-Pd}_3\text{P@C}$ catalyst exhibits a mass activity of $1.66 \text{ mA } \mu\text{g}_{\text{Pd}}^{-1}$, significantly higher than $\text{Pd}_3\text{P@C}$ ($0.45 \text{ mA } \mu\text{g}_{\text{Pd}}^{-1}$), Pd@C ($0.073 \text{ mA } \mu\text{g}_{\text{Pd}}^{-1}$), commercial Pd/C ($0.123 \text{ mA } \mu\text{g}_{\text{Pd}}^{-1}$) and commercial Pt/C ($0.3 \text{ mA } \mu\text{g}_{\text{Pt}}^{-1}$). As the presence of Pd could interfere the hydrogen adsorption/desorption potential region (H_{upd}), we performed CO stripping voltammetry to measure the electrochemical active surface area (ECSA) values, revealing the ECSA value of $196.4 \text{ m}^2 \text{ g}^{-1}$ for $V_p\text{-Pd}_3\text{P@C}$, which is larger than those of $\text{Pd}_3\text{P@C}$ ($129.0 \text{ m}^2 \text{ g}^{-1}$), Pd@C ($71.9 \text{ m}^2 \text{ g}^{-1}$), commercial Pd/C ($59.5 \text{ m}^2 \text{ g}^{-1}$) and commercial Pt/C ($122.1 \text{ m}^2 \text{ g}^{-1}$) (Figs. 4(e) and S5). The ECSA values of other samples were summarized in Table S2. Also, $V_p\text{-Pd}_3\text{P@C}$ exhibits the highest specific activity (SA) of 0.85 mA cm^{-2} , surpassing the SA values of the other samples. Overall, the $V_p\text{-Pd}_3\text{P@C}$ demonstrates superior electrocatalytic performance in terms of j_0 , j_k at 50 mV, MA, ECSA and SA (Fig. 4(e) and Table S2). When compared with other recently reported catalysts (Fig. 4(f) and Table S3), $V_p\text{-Pd}_3\text{P@C}$ also shows distinct advantages on MA and j_0 .

In hydrogen fuel cells, anodes with PGM catalysts, especially Pt, are susceptible to poisoning in the presence of CO. CO adsorbs tightly on the Pt surface, blocking active sites for hydrogen adsorption and dissociation [44]. In Fig. 4(g), it can be observed that the Pt/C catalyst exhibits a large drop in activity with 1000 ppm CO in the H_2 fuel, suggesting CO poison the sites of H_2 oxidation [41]. The current density of Pt/C gradually increases when the potential reaches 0.4 V, indicating a complete shift in the reaction from HOR to CO oxidation, consistent with the literature [45,46]. In striking contrast, $V_p\text{-Pd}_3\text{P@C}$ maintains high HOR activity even at the same CO concentration, demonstrating good resistance to CO poisoning. This is attributed to the phosphorus vacancy in $V_p\text{-Pd}_3\text{P@C}$, which confer protection to Pd sites against poisoning and deactivation caused by strong CO adsorption during catalysis [47]. Apart from the activity and CO tolerance, long-term stability is another key figure of merit for practical application. Fig. 4(h)

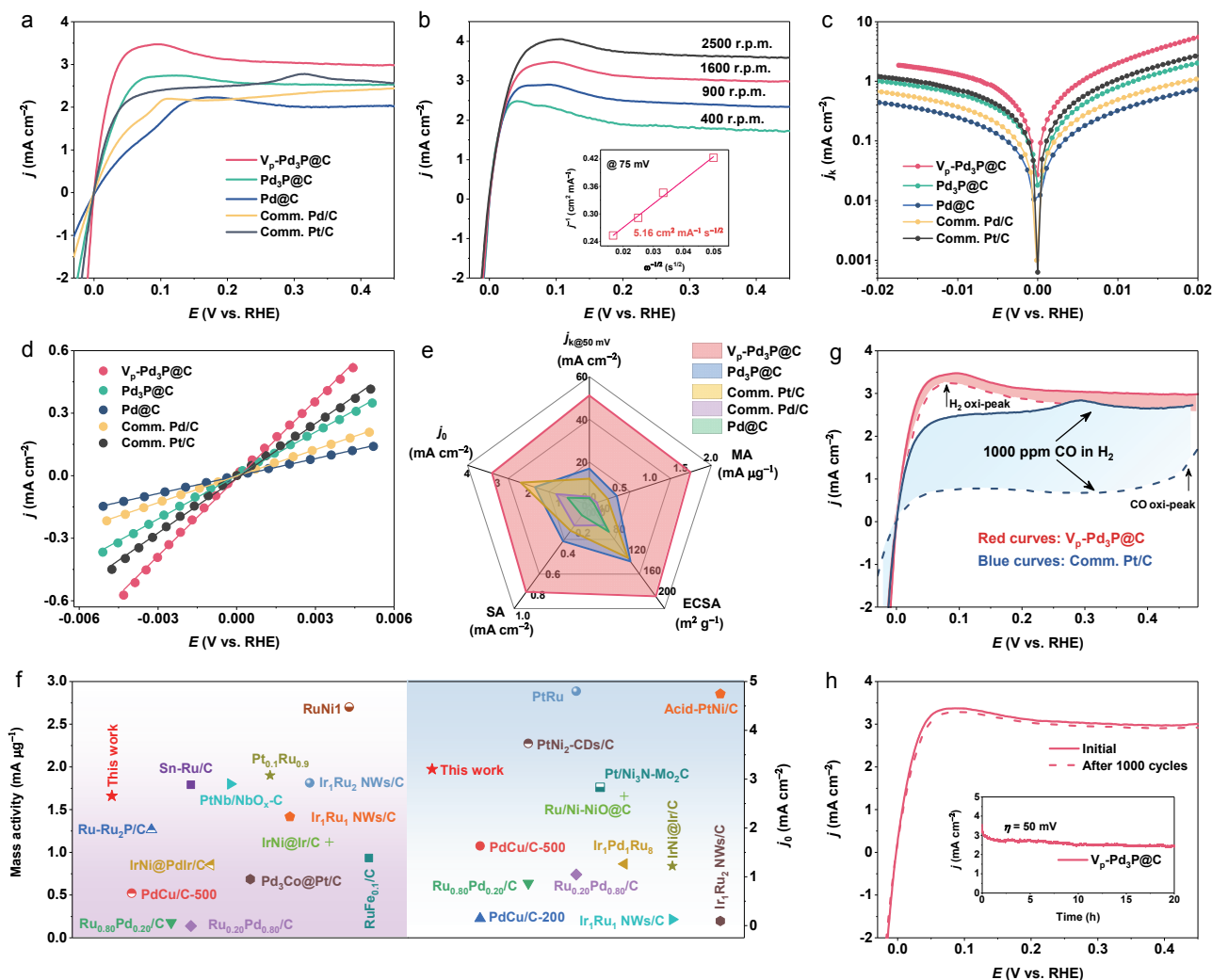


Fig. 4. (a) HOR polarization curves of V_p -Pd₃P@C, Pd₃P@C, Pd@C, commercial Pd/C and commercial Pt/C, respectively. (b) HOR polarization curves for V_p -Pd₃P@C at various rotation speeds. Inset in b shows corresponding Koutecky-Levich plots at an overpotential of 75 mV. (c) Tafel plots. (d) Linear current potential region around the equilibrium potential of studied catalysts. (e) Comparison of apparent exchange current density (j_0), kinetic current density (j_k) at 50 mV, mass activity (MA) at 50 mV, ECSA, and specific activity (SA) at 50 mV of the comparative catalysts. (f) Comparison of mass activity at 50 mV and j_0 with other recently reported excellent HOR catalysts. (g) HOR polarization curves for V_p -Pd₃P@C and Pt/C in H₂-saturated 0.1 mol L⁻¹ KOH with (dashed lines) and without (solid lines) the presence of 1000 ppm CO. (h) HOR polarization curves for V_p -Pd₃P@C in H₂-saturated 0.1 mol L⁻¹ KOH before and after 1000 cycles, respectively. Inset shows chronoamperometry ($j-t$) responses recorded on V_p -Pd₃P@C at 50 mV.

shows the polarization curves of V_p -Pd₃P@C before and after accelerated durability tests (ADT), and the two polarization curves coincide well. Additionally, we also evaluated the ability of V_p -Pd₃P@C to continuously catalyze the HOR by chronoamperometry ($j-t$) at 50 mV, which can sustain HOR reactivity without obvious degradation throughout the test. Additionally, we examined the HRTEM image of post-test V_p -Pd₃P@C to assess the resilience of the Pd₃P lattice structure following the ADT (Fig. S6). The distinct lattice fringe spacings, measuring 0.23 nm and linked to the (220) plane of Pd₃P, are still evident. This testifies that the phosphorus vacancy defect remains unintrusive to the Pd₃P lattice structure's stability amidst heightened current and alkaline conditions during HOR. Furthermore, SEM and XPS characterizations display that the morphology and structural integrity of V_p -Pd₃P@C are well maintained after the stability test, demonstrating its robust structure to with-

stand alkali corrosion during HOR without structural deterioration (Figs. S7 and S8).

3.3. CO-tolerance evaluation

The theoretical model of CO-metal bonding explains the electron structures involved (Fig. 5(a)) [4,48]. Partial electrons in the 5s orbitals transferred into the metal d -orbitals, alongside fed back from metal d -orbitals into CO 2 π^* orbitals [17]. Therefore, the ability of our developed Pd-based catalysts to resist CO poisoning can be reflected in their electron structure. Accordingly, we undertook all-in vacuum ultraviolet photoelectron spectroscopy (UPS) measurements to explore the surface electronic property [49]. In Fig. 5(b), the cutoff level (E_{cutoff}) is confirmed, and the work function is calculated. The work function sequence is as follows: V_p -Pd₃P@C (4.82 eV) >

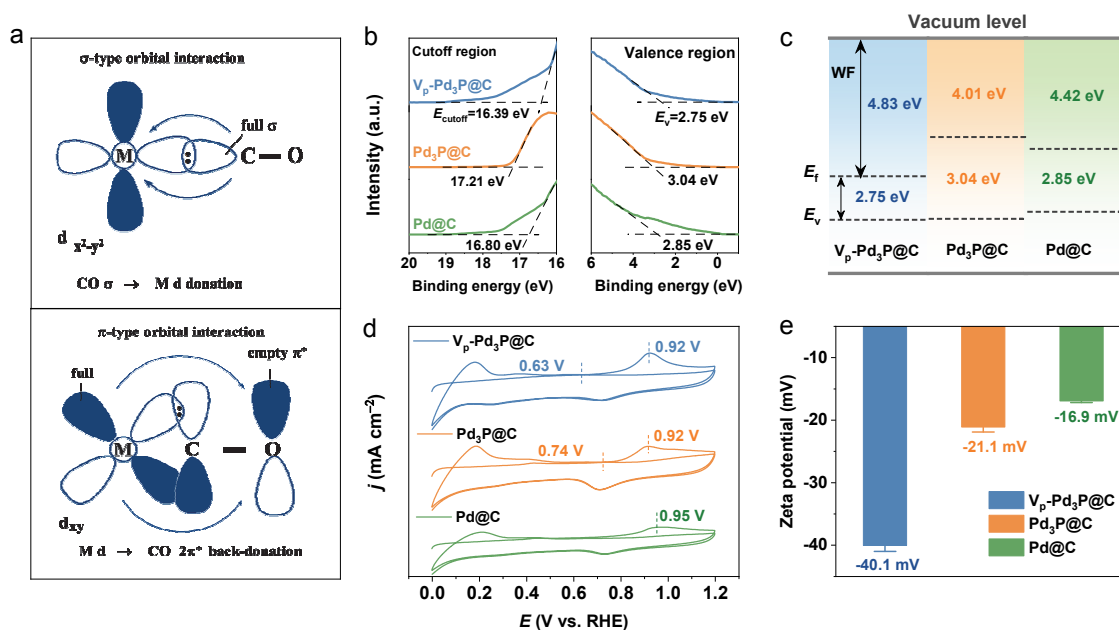


Fig. 5. (a) Schematic diagram of σ -type/ π -type orbital interactions between metal catalysts and CO molecules. (b) UPS spectra. (c) Band structure alignment of the $V_p\text{-Pd}_3\text{P@C}$, $\text{Pd}_3\text{P@C}$, and Pd@C . (d) CO stripping curves in N_2 -saturated 0.1 mol L^{-1} KOH of $V_p\text{-Pd}_3\text{P@C}$, $\text{Pd}_3\text{P@C}$, and Pd@C . (e) Zeta potential of $V_p\text{-Pd}_3\text{P@C}$, $\text{Pd}_3\text{P@C}$, and Pd@C . Error bars represent the standard deviation for triplicated experiments.

Pd@C (4.42 eV) > $\text{Pd}_3\text{P@C}$ (4.01 eV). A higher work function implies that electrons are less likely to escape, indicating that the catalyst is more likely to receive electrons. Therefore, we further conjecture that the surface valence state of $V_p\text{-Pd}_3\text{P@C}$ is more positive than that of $\text{Pd}_3\text{P@C}$ and Pd@C , that is, $V_p\text{-Pd}_3\text{P@C}$ contains more-empty d -orbitals than $\text{Pd}_3\text{P@C}$ and Pd@C , in conformity with the XPS results [17]. As anticipated, $V_p\text{-Pd}_3\text{P@C}$, with emptier d -orbitals, leads to reduced back-donation of d -band electrons to CO $2\pi^*$ states, thereby weakening the bond strength of Pd-CO compared with $\text{Pd}_3\text{P@C}$ and Pd@C , which is the reason for its good CO tolerance property. These theoretical predictions align with our experimental data (Fig. S9). Besides, ionization potential (E_i) can be informative concerning the electron-donating and electron-accepting capabilities of electrocatalysts and can be calculated by $E_i = WF + E_v$. Phosphorus has an electron-deficient valence shell, with relatively lower electronegativity than carbon [50]. $\text{Pd}_3\text{P@C}$ has a lower ionization potential (7.05 eV) compared to Pd@C (7.27 eV), signifying that phosphorus tends to donate electrons to the carbon support, resulting in a partial positive charge on phosphorus [50]. Typically, vacancy could unlock the huge potential that exists for tailoring surface electronegativity, charge concentration, and redistribution [51]. As a result, the carbon matrix is biased toward the donation of electron to phosphorus when introducing higher concentration of phosphorus vacancies, corresponding to the higher ionization potential of $V_p\text{-Pd}_3\text{P@C}$ (7.58 eV) (Fig. 5(c)) [52]. As known that whether the dopant is partial positive and partial negative charges, it is in favor of creating a new equilibrium state of catalyst [50]. Thus, the introduction of P species and vacancy break the charge balance established by Pd and carbon matrix, leading to the profound charge redistribution of Pd active sites in $\text{Pd}_3\text{P@C}$

and $V_p\text{-Pd}_3\text{P@C}$, which in turn, regulates the HOR intermediates adsorption process, boosting the HOR activity and rendering these two catalysts follow different HOR mechanism, as discussed in more detail in the DFT results below.

3.4. HOR enhancement mechanism

In alkaline HOR, both HBE and OHBE are considered activity descriptors [41,53]. However, monitoring OH binding on the catalyst surface remains an active research area. It has been reported that CO stripping is propelled by the reaction between the formed OH_{ads} and CO_{ads} ($\text{CO}_{\text{ads}} + \text{OH}_{\text{ads}} \rightarrow \text{CO}_2 + \text{H}_2\text{O}$, CO_{ads} and OH_{ads} represent the radicals adsorbed on the active sites). Therefore, we executed CO-stripping experiments to assess the OH binding on our catalyst surface [54,55]. As depicted in Fig. 5(d), the CO-stripping peaks for both $V_p\text{-Pd}_3\text{P@C}$ (0.92 V) and $\text{Pd}_3\text{P@C}$ (0.92 V) are more negative compared to Pd@C (0.95 V). This indicates a stronger OH_{ads} binding affinity for $V_p\text{-Pd}_3\text{P@C}$ and $\text{Pd}_3\text{P@C}$. Notably, the onset potential for the CO stripping peak in $V_p\text{-Pd}_3\text{P@C}$ (0.63 V) precedes that of $\text{Pd}_3\text{P@C}$ (0.74 V), affirming that phosphorus vacancy introduction considerably boosts OH_{ads} binding energy in $V_p\text{-Pd}_3\text{P@C}$ (Fig. S10). Additionally, the adsorption behavior of hydroxyl species on the catalysts is investigated using zeta potential, which reflects the charge density of the catalyst's surface and provides insights into the interaction between the catalysts and OH species [18]. Figs. 5(e) and S11 clearly disclose that $V_p\text{-Pd}_3\text{P@C}$ exhibits optimized adsorption of OH, with a more negative potential of -40.1 mV compared to $\text{Pd}_3\text{P@C}$ (-21.1 mV) and Pd@C (-16.9 mV) [17]. Overall, the CO-stripping and zeta potential measurements demonstrate that the strengthened OHBE of $V_p\text{-Pd}_3\text{P@C}$ could boost the rate-limiting Volmer reaction for

robust HOR catalysis.

To gain insight into the mechanism behind the enhancement of HOR, DFT calculations were performed based on crystal configurations, and the optimized model diagrams were depicted (Figs. S12–S15). Fig. 6(a) shows the significant charge redistribution of V_p -Pd₃P@C. A slice perspective of the differential charge density provides a clearer view of this phenomenon, revealing electron gathering area in Pd–P bonds close to the P atoms, while the electrons are depleted around the Pd atoms accordingly (Fig. 6(b)). This observation aligns with the XPS results. Modulating the electronic structures leads to a noticeable shift in the *d*-band center of Pd sites. According to the *d*-band theory, the position of *d*-band center reflects the binding strength of intermediate adsorbates [21]. The projected partial density of states (PDOS) of surface Pd atoms in the three types of catalysts were investigated (Fig. 6(c)), and the *d*-band center value of Pd in V_p -Pd₃P@C (–2.13 eV) falls between that of Pd₃P@C (–2.30 eV) and Pd@C (–1.64 eV). This shift is attributed to the charge transfer caused by constructing the pal-

adium phosphide and introducing phosphorus vacancies, resulting in synergistic optimization of both H_{ads} and OH_{ads} binding strengths on the V_p -Pd₃P@C surface [56]. In the bifunctional mechanism of HOR, the Volmer process is the RDS, regardless of whether the subsequent step is the Heyrovsky or Tafel route [57]. The crux of bifunctional theory is that OH_{ads} in the vicinity of H_{ads} facilitates the oxidative desorption of H_{ads} , substantially promoting the key Volmer step [20]. Thus, the alkaline HOR activity is synergistically affected by HBE and OHBE. We then computed HBE and OHBE to elucidate the origin of discrepancies in catalyst performance. It is shown that the Pd₃P@C exhibits a weakened HBE of –0.73 eV compared to pure Pd@C (–0.83 eV), indicating the modest regulation of hydrogen adsorption due to the synergistic electronic effect between Pd and P species (Fig. 6(d)) [58]. Remarkably, V_p -Pd₃P@C exhibits an even smaller HBE value of –0.28 eV, corroborating that the rich phosphorus vacancy can shuffle the H_{ads} intermediates for optimal HBE. In parallel, we observed a stronger OHBE of V_p -Pd₃P@C (–0.93 eV) compared to Pd₃P@C (–0.82 eV) and

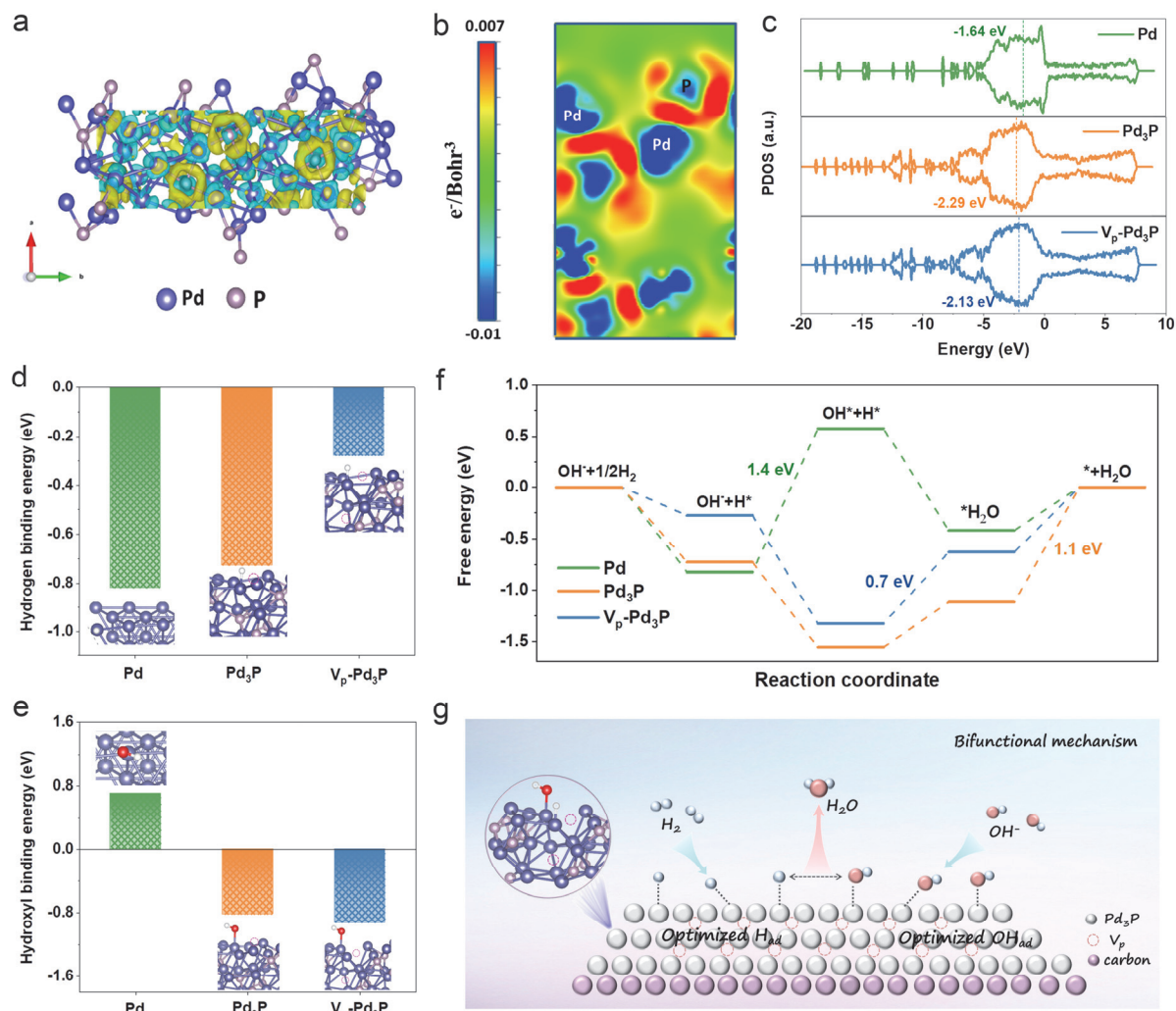


Fig. 6. (a) Charge-density distribution of the V_p -Pd₃P@C model, yellow and cyan areas indicate electron accumulation and depletion. (b) 2D charge difference isosurface based on DFT analysis, red is the electron-rich area while blue is the deficient area. (c) The PDOS of Pd 4*d* in V_p -Pd₃P@C, Pd₃P@C and Pd@C (each *d*-band center is marked by a dashed line). (d) Hydrogen binding energy on V_p -Pd₃P@C, Pd₃P@C, and Pd@C models. (e) Hydroxyl binding energy on V_p -Pd₃P@C, Pd₃P@C, and Pd@C models. (f) The reaction pathways of V_p -Pd₃P@C, Pd₃P@C, and Pd@C for alkaline HOR. (g) Schematic illustration of HOR catalysis on the V_p -Pd₃P@C.

Pd@C (0.71 eV) (Fig. 6(e)), which originates from phosphorus vacancy that contribute to the capture of hydroxyl species [13,58]. As a result, V_p -Pd₃P@C delivers optimal HBE and OHBE, which greatly accelerates the Volmer step during the alkaline HOR process through a bifunctional mechanism to achieve high HOR performance. Furthermore, the free energy profile and reaction pathway on various catalysts are illustrated in Fig. 6(f). The results suggest that H adsorption and H₂O formation steps on Pd@C are exergonic, but OH adsorption and H₂O desorption are endothermic, with potential barriers of 1.4 and 0.42 eV, respectively, suggesting that the OH adsorption step is the RDS for Pd@C. By introducing P species and constructing phosphorus vacancies, both H and OH adsorption steps become exergonic on V_p -Pd₃P@C and Pd₃P@C. The subsequent H₂O formation step is endothermic, with a barrier of 0.7 eV for V_p -Pd₃P@C and 0.45 eV for Pd₃P@C. The final H₂O desorption process is endothermic and considerably more difficult for Pd₃P@C, with a barrier of 1.1 eV, compared to 0.63 eV for V_p -Pd₃P@C. Thus, the H₂O formation (Volmer step) is considered the RDS for V_p -Pd₃P@C (0.7 eV), in line with the prevailing views in the literature [8,20,59], while the H₂O desorption step is the RDS for Pd₃P@C (1.1 eV). Theoretical simulation results demonstrate that V_p -Pd₃P@C, with rich vacancies, gives rise to optimal HBE and OHBE that improve the HOR energetics. A visual and direct reaction mechanism of HOR catalysis on the V_p -Pd₃P@C model is illustrated in Fig. 6(g) to provide a better understanding of the reaction process.

Taken together, the enhanced electrocatalytic properties of V_p -Pd₃P@C can be attributed to several factors. Firstly, the hollow bowl-like structure of V_p -Pd₃P@C allows for unobstructed entry of reactants into the cavities, ensuring efficient contact with active sites and promoting the HOR process. Secondly, the strong electron interaction between Pd and P in V_p -Pd₃P@C reduces the energetic barrier and accelerates the HOR kinetics. Thirdly, the presence of abundant phosphorus vacancy disrupts the original periodic crystal structure and creates a new electronic structure. This new structure suppresses the back donation of Pd *d*-electron to CO 2π* and enhances CO tolerance capability of V_p -Pd₃P@C. Finally, the synergistic interplay of optimal HBE and OHBE on the surface of V_p -Pd₃P@C greatly facilitates the Volmer step, which is the RDS in the alkaline HOR process.

4. Conclusions

In conclusion, we have designed distinctive Pd_xP_y hollow hemispheres with tunable crystal phases and phosphorus vacancy leveraging on a mild phosphating strategy, and established a clear correlation between the concentration of phosphorus vacancy and HOR activity. Phosphorus vacancy acts as an electronic structure regulator, optimizing the bonding strength between Pd and HOR intermediates, and shifting the HOR activity toward the apex of the volcano curve. Specifically, the vacancy defect-rich V_p -Pd₃P@C catalyst manifests vastly superior HOR mass activity and exchange current density relative to Pd₃P@C and commercial Pt/C, respectively. To its credit, V_p -Pd₃P@C can continuously catalyze the H₂ oxidation during a

20-hour testing period without obvious degradation and demonstrate high CO tolerance. DFT calculations reveal that the favorable electronic structure controlled by phosphorus vacancy enables the optimized HBE and OHBE, resulting in a switch of the RDS from desorption of adsorbed H₂O to the formation of H₂O, thereby accelerating the rate-limiting Volmer step. Meanwhile, the inter-regulated *d*-band center, achieved through the redistribution of local charge density, effectively suppresses Pd 4*d* → CO 2π* back donation, leading to a high resilience to CO poisoning. This work presents a new strategy for designing highly active precious metal-based catalysts using defect engineering, which can significantly enhance the hydrogen oxidation performance for the commercialization of AEMFCs.

Notes

The authors declare no conflict of interest.

Electronic supporting information

Supporting information is available in the online version of this article.

References

- [1] C. Sun, P. Zhao, Y. Yang, Z. Li, W. Sheng, *ACS Catal.*, **2022**, 12, 11830–11837.
- [2] L. Su, D. Gong, N. Yao, Y. Li, Z. Li, W. Luo, *Adv. Funct. Mater.*, **2021**, 31, 2106156.
- [3] J. Liao, W. Ding, S. Tao, Y. Nie, W. Li, G. Wu, S. Chen, L. Li, Z. Wei, *Chin. J. Catal.*, **2016**, 37, 1142–1148.
- [4] H. Cheng, J. Xia, M. Wang, C. Wang, R. Gui, X. Cao, T. Zhou, X. Zheng, W. Chu, H. Wu, Y. Xie, C. Wu, *J. Am. Chem. Soc.*, **2022**, 144, 22018–22025.
- [5] Y. Yang, F. Gao, X. Zhang, S. Qin, L. Zheng, Y. Wang, J. Liao, Q. Yang, M. Gao, *Angew. Chem. Int. Ed.*, **2022**, 61, e202208040.
- [6] P. Han, N. Yao, W. Zuo, W. Luo, *Chin. J. Catal.*, **2022**, 43, 1527–1534.
- [7] Z. Zhang, H. Liu, L. Ni, Z.-L. Zhao, H. Li, *J. Energy Chem.*, **2022**, 72, 176–185.
- [8] J. Zheng, W. Sheng, Z. Zhuang, B. Xu, Y. Yan, *Sci. Adv.*, **2016**, 2, e1501602.
- [9] L. Fu, F. Yang, Y. Hu, Y. Li, S. Chen, W. Luo, *Sci. Bull.*, **2020**, 65, 1735–1742.
- [10] L. Fu, Y. Li, N. Yao, F. Yang, G. Cheng, W. Luo, *ACS Catal.*, **2020**, 10, 7322–7327.
- [11] P. S. Lamoureux, A. R. Singh, K. Chan, *ACS Catal.*, **2019**, 9, 6194–6201.
- [12] Y. Qiu, L. Xin, Y. Li, I. T. McCrum, F. Guo, T. Ma, Y. Ren, Q. Liu, L. Zhou, S. Gu, M. J. Janik, W. Li, *J. Am. Chem. Soc.*, **2018**, 140, 16580–16588.
- [13] Y. Yang, Y. Huang, S. Zhou, Y. Liu, L. Shi, T. T. Isimjan, X. Yang, *J. Energy Chem.*, **2022**, 72, 395–404.
- [14] X. Wang, L. Zhao, X. Li, Y. Liu, Y. Wang, Q. Yao, J. Xie, Q. Xue, Z. Yan, X. Yuan, W. Xing, *Nat. Commun.*, **2022**, 13, 1596.
- [15] A. R. Poerwoprajitno, L. Gloag, J. Watt, S. Cheong, X. Tan, H. Lei, H. A. Tahini, A. Henson, B. Subhash, N. M. Bedford, B. K. Miller, P. B. O'Mara, T. M. Benedetti, D. L. Huber, W. Zhang, S. C. Smith, J. J. Gooding, W. Schuhmann, R. D. Tilley, *Nat. Catal.*, **2022**, 5, 231–237.
- [16] A. Garg, M. Milina, M. Ball, D. Zanchet, S. T. Hunt, J. A. Dumesic, Y.

Graphical Abstract

Chin. J. Catal., 2024, 56: 176–187 doi: 10.1016/S1872-2067(23)64570-X

Uleashing efficient and CO-resilient alkaline hydrogen oxidation of Pd₃P through phosphorus vacancy defect engineering

Yuting Yang, Luyan Shi, Qinrui Liang, Yi Liu, Jiaxin Dong, Tayirjan Taylor Isimjan*, Bao Wang, Xiulin Yang*

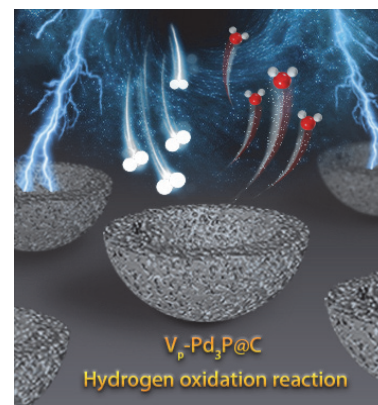
Guangxi Normal University, China;

Sun Yat-sen University, China;

Institute of Process Engineering, Chinese Academy of Sciences, China;

King Abdullah University of Science and Technology (KAUST), Saudi Arabia

Phosphorus vacancy has been created, and its effect to regulate the *d*-band center of Pd active centers for activating key intermediates in HOR is demonstrated. As a proof of utility, the obtained phosphorus-vacancy-rich Pd₃P@C (V_p-Pd₃P@C) catalyst with bowl-like structure exhibits high HOR activity and resilience to CO poisoning.



- Román-Leshkov, *Angew. Chem. Int. Ed.*, **2017**, 56, 8828–8833.
- [17] L. Su, X. Fan, Y. Jin, H. Cong, W. Luo, *Small*, **2023**, 19, 2207603.
- [18] L. Su, Y. Zhao, Y. Jin, Z. Liu, H. Cui, W. Luo, *Adv. Funct. Mater.*, **2022**, 32, 2113047.
- [19] B. Zhang, G. Zhao, B. Zhang, L. Xia, Y. Jiang, T. Ma, M. Gao, W. Sun, H. Pan, *Adv. Mater.*, **2021**, 33, 2105400.
- [20] Z. Yao, T. Tang, Z. Jiang, L. Wang, J. Hu, L. Wan, *ACS Nano*, **2022**, 16, 5153–5183.
- [21] L. Su, Y. Jin, D. Gong, X. Ge, W. Zhang, X. Fan, W. Luo, *Angew. Chem. Int. Ed.*, **2022**, 62, e202215585.
- [22] Y. Kuang, W. Qiao, F. Yang, L. Feng, *J. Energy Chem.*, **2023**, 85, 447–454.
- [23] J. Liu, Z. Luo, J. Li, X. Yu, J. Llorca, D. Nasioiu, J. Arbiol, M. Meyns, A. Cabot, *Appl. Catal. B*, **2019**, 242, 258–266.
- [24] H. Zhang, M. Yu, H. Song, O. Noonan, J. Zhang, Y. Yang, L. Zhou, C. Yu, *Chem. Mater.*, **2015**, 27, 6297–6304.
- [25] J. Duan, S. Chen, C.A. Ortíz-Ledón, M. Jaroniec, S.-Z. Qiao, *Angew. Chem. Int. Ed.*, **2020**, 59, 8181–8186.
- [26] G. Kresse, J. Furthmüller, *Comput. Mater. Sci.*, **1996**, 6, 15–50.
- [27] G. Kresse, J. Furthmüller, *Phys. Rev. B*, **1996**, 54, 11169–11186.
- [28] J. P. Perdew, K. Burke, M. Ernzerhof, *Phys. Rev. Lett.*, **1996**, 77, 3865–3868.
- [29] P. E. Blöchl, *Phys. Rev. B*, **1994**, 50, 17953–17979.
- [30] T. Dong, C. Ling, L. Fu, Y. Xue, Y. Pan, Y. Zhang, C. Zhu, *J. Hazard. Mater.*, **2023**, 445, 130562.
- [31] J. Du, A. Chen, X. Gao, Y. Zhang, H. Lv, *Carbon*, **2022**, 191, 67–74.
- [32] Y. Gao, K. Wang, C. Xu, H. Fang, H. Yu, H. Zhang, S. Li, C. Li, F. Huang, *Appl. Catal. B*, **2023**, 330, 122627.
- [33] T. Yang, Y. Xia, T. Mao, Q. Ding, Z. Wang, Z. Hong, J. Han, D. Peng, G. Yue, *Adv. Funct. Mater.*, **2022**, 32, 2209876.
- [34] Z. Yang, W. Lai, B. He, J. Wang, F. Yu, Q. Liu, M. Liu, S. Zhang, W. Ding, Z. Lin, H. Huang, *Adv. Energy Mater.*, **2023**, 13, 2300881.
- [35] J. Wu, Y. Zhou, H. Nie, K. Wei, H. Huang, F. Liao, Y. Liu, M. Shao, Z. Kang, *J. Energy Chem.*, **2022**, 66, 61–67.
- [36] W. Li, D. Wang, Y. Zhang, L. Tao, T. Wang, Y. Zou, Y. Wang, R. Chen, S. Wang, *Adv. Mater.*, **2020**, 32, 1907879.
- [37] C. Jin, J. Li, K. Zhang, Habibullah, G. Xia, C. Wu, Y. Wang, W. Cen, Y. Chen, Y. Yan, Y. Chen, *Nano Energy*, **2022**, 99, 107360.
- [38] Z. Guo, R. Wang, Y. Guo, J. Jiang, Z. Wang, W. Li, M. Zhang, *ACS Catal.*, **2022**, 12, 15193–15206.
- [39] F. Luo, Q. Zhang, X. Yu, S. Xiao, Y. Ling, H. Hu, L. Guo, Z. Yang, L. Huang, W. Cai, H. Cheng, *Angew. Chem. Int. Ed.*, **2018**, 57, 14862–14867.
- [40] T. Xu, D. Jiao, L. Zhang, H. Zhang, L. Zheng, D. J. Singh, J. Zhao, W. Zheng, X. Cui, *Appl. Catal. B*, **2022**, 316, 121686.
- [41] Y. Duan, Z.-Y. Yu, L. Yang, L. Zheng, C. Zhang, X. Yang, F. Gao, X. Zhang, X. Yu, R. Liu, H. Ding, C. Gu, X. Zheng, L. Shi, J. Jiang, J. Zhu, M. Gao, S. Yu, *Nat. Commun.*, **2020**, 11, 4789.
- [42] Y. Duan, X. Zhang, F. Gao, Y. Kong, Y. Duan, X. Yang, X. Yu, Y. Wang, S. Qin, Z. Chen, R. Wu, P. Yang, X. Zheng, J. Zhu, M. Gao, T. Lu, Z. Yu, S. Yu, *Angew. Chem. Int. Ed.*, **2023**, 62, e202217275.
- [43] X. Tian, P. Zhao, W. Sheng, *Adv. Mater.*, **2019**, 31, 1808066.
- [44] S. Qin, Y. Duan, X. Zhang, L. Zheng, F. Gao, P. Yang, Z. Niu, R. Liu, Y. Yang, X. Zheng, J. Zhu, M. Gao, *Nat. Commun.*, **2021**, 12, 2686.
- [45] Y. Y. Zhou, Z. Y. Xie, J. X. Jiang, J. Wang, X. Y. Song, Q. He, W. Ding, Z. D. Wei, *Nat. Catal.*, **2020**, 3, 454–462.
- [46] F. Gao, S. Liu, J. Ge, X. Zhang, L. Zhu, Y. Zheng, Y. Duan, S. Qin, W. Dong, X. Yu, R. Bao, P. Yang, Z. Niu, Z. Ding, W. Liu, S. Lan, M. Gao, Y. Yan, S. Yu, *Nat. Catal.*, **2022**, 5, 993–1005.
- [47] X. Wu, Y. Zhang, Y. Yang, G. Fu, F. Si, J. Chen, M. Ahmad, Z. Zhang, C. Ye, J. Zhang, X. Fu, J. Luo, *Chem. Eng. J.*, **2023**, 452, 139057.
- [48] F. Gao, M. Gao, *Acc. Chem. Res.*, **2023**, 56, 1445–1457.
- [49] W. Ren, X. Tan, C. Jia, A. Krammer, Q. Sun, J. Qu, S. C. Smith, A. Schueler, X. Hu, C. Zhao, *Angew. Chem. Int. Ed.*, **2022**, 61, e202203335.
- [50] J. Zhang, J. Zhang, F. He, Y. Chen, J. Zhu, D. Wang, S. Mu, H. Y. Yang, *Nano-Micro Lett.*, **2021**, 13, 65.
- [51] Z. Y. Yu, Y. Duan, J. D. Liu, Y. Chen, X. K. Liu, W. Liu, T. Ma, Y. Li, X. S. Zheng, T. Yao, M. R. Gao, J. F. Zhu, B. J. Ye, S.H. Yu, *Nat. Commun.*, **2019**, 10, 2799.
- [52] J. Cheng, C. Lyu, H. Li, J. Wu, Y. Hu, B. Han, K. Wu, M. Hojamberdiev, D. Geng, *Appl. Catal. B*, **2023**, 327, 122470.
- [53] Y. Qiu, X. Xie, W. Li, Y. Shao, *Chin. J. Catal.*, **2021**, 42, 2094–2104.
- [54] Y. Men, X. Su, P. Li, Y. Tan, C. Ge, S. Jia, L. Li, J. Wang, G. Cheng, L. Zhuang, S. Chen, W. Luo, *J. Am. Chem. Soc.*, **2022**, 144, 12661–12672.
- [55] L. Chen, L. Lu, H. Zhu, Y. Chen, Y. Huang, Y. Li, L. Wang, *Nat. Commun.*, **2017**, 8, 14136.
- [56] L. Wu, L. Su, Q. Liang, W. Zhang, Y. Men, W. Luo, *ACS Catal.*, **2023**, 13, 4127–4133.
- [57] J. Zhang, X. Liu, Y. Ji, X. Liu, D. Su, Z. Zhuang, Y.-C. Chang, C.-W. Pao, Q. Shao, Z. Hu, X. Huang, *Nat. Commun.*, **2023**, 14, 1761.

[58] F. Yang, X. Bao, P. Li, X. Wang, G. Cheng, S. Chen, W. Luo, *Angew. Chem. Int. Ed.*, **2019**, 58, 14179–14183.

[59] J. Durst, A. Siebel, C. Simon, F. Hasché, J. Herranz, H. A. Gasteiger, *Energy Environ. Sci.*, **2014**, 7, 2255–2260.

构筑富含磷空位缺陷的磷化钯催化剂实现高效和抗CO毒化的碱性氢氧化反应

杨玉婷^{a,b,1}, 石路岩^{a,1}, 梁沁睿^a, 刘奕^a, 董家新^a, Tayirjan Taylor Isimjan^{d,*}, 王宝^c, 杨秀林^{a,*}

^a广西师范大学化学与药学院, 广西低碳能源材料重点实验室, 广西桂林541004, 中国

^b中山大学环境科学与工程学院, 广东广州510275, 中国

^c中国科学院过程工程研究所, 生化工程国家重点实验室, 北京100190, 中国

^d阿卜杜拉国王科技大学的沙特阿拉伯基础工业公司, 图瓦勒, 沙特阿拉伯

摘要: 碱性阴离子交换膜燃料电池(AEMFCs)可以直接将氢的化学能转化为电能, 被认为是新兴绿色氢经济的基石技术。但其阳极氢氧化反应(HOR)动力学缓慢, 严重依赖于Pt基催化剂。由于Pt基催化剂极易被CO毒化、动力学过程复杂以及价格昂贵, 极大限制了其商业化应用。因此, 亟需开发高效、稳定和抗CO毒化能力强的新型HOR催化剂。Pd具有与Pt相似的氢键结合能, 并且比Pt储量丰富, 有望成为实现HOR的候选催化剂。然而, Pd的本征催化活性和Pt相比仍有很大差距。近年来, 磷化钯因具有功能多样性和高催化活性被广泛关注。此外, 缺陷工程可以有效调控催化剂的表面结构, 改善中间体的吸附强度, 提高催化剂的催化活性。因此, 构建富含缺陷的磷化钯催化剂有望提高其HOR的性能。然而, 该方向研究较少, 反应机理尚不清楚。因此, 阐明空位缺陷对于提高磷化钯催化剂HOR性能的作用机制, 对促进AEMFCs电催化反应具有重要意义。

本文通过溶胶-凝胶法以及低温磷化策略合成了一种碗状半球结构的富含磷空位Pd₃P@C (V_p-Pd₃P@C)催化剂, 并用于碱性HOR。在磷化过程中, 通过调整Pd前驱体和磷源比例以及煅烧温度, 在碗状半球载体上合成具有不同晶相组成(Pd/Pd₃P@C, Pd₃P₁₂@C, Pd₃P@C, 和Pd₅P₂@C)的Pd_xP_y@C催化剂。扫描电镜和透射电镜证实了催化剂为碗状半球形貌。利用电子顺磁共振波谱研究了Pd_xP_y@C催化剂的磷空位浓度, 结果表明, Pd/P比例为1:3时, 在350 °C下煅烧得到的V_p-Pd₃P@C具有最高的磷空位浓度。X射线光电子能谱证实了磷空位促进了d-p轨道杂化, 增强了Pd和磷之间的电子相互作用。电化学测试结果表明, V_p-Pd₃P@C具有最高的HOR性能, V_p-Pd₃P@C在50 mV的质量活性为1.66 mA μg_{Pd}⁻¹, 交换电流密度为3.2 mA cm⁻², 优于Pd₃P (0.45 mA μg_{Pd}⁻¹, 1.78 mA cm⁻²)和商业Pt/C (0.3 mA μg_{Pt}⁻¹, 2.29 mA cm⁻²)。同时, 该催化剂在50 mV的电位下能稳定运行20 h。此外, 即使在CO浓度高达1000 ppm时, V_p-Pd₃P@C催化剂仍表现出较好的HOR活性。紫外光电子能谱证实了V_p-Pd₃P@C中的Pd原子呈现缺电子状态, 这不利于Pd 4d轨道对CO 2π*轨道的电子反馈, 降低了Pd和CO的键合强度, 进而减弱了Pd对CO分子的吸附, 从而增强了其抗CO中毒的能力。密度泛函理论计算结果表明, 相较于磷空位浓度较少的Pd₃P@C催化剂, 富含磷空位缺陷的V_p-Pd₃P@C催化剂能够优化和平衡反应中间体(H_{ads}和OH_{ads})的吸附强度, 使速率决定步骤从H₂O*的解吸转换到H₂O的形成, 促进了Volmer反应(H_{ads} + OH_{ads} → H₂O + 2*sites)的进行, 进而提升了催化活性。系统实验和表征结果表明, V_p-Pd₃P@C较好的HOR性能可归因于以下3个因素: (1) 空心碗状结构大大地增加了固-液-气三相接触点, 加速了HOR的传质过程; (2) 磷空位产生的局部反应活性和有利的电子结构优化了H_{ads}和OH_{ads}的吸附强度, 极大地促进了Volmer步骤; (3) 丰富的磷空位打破了原有的周期性晶体结构, 形成了新的电子结构, 有效地抑制了电子从Pd 4d轨道到CO 2π*轨道的反馈, 提高了V_p-Pd₃P@C对CO的耐受能力。

综上, 本文通过缺陷工程策略调控了V_p-Pd₃P@C中活性位点与HOR关键中间体的相互作用, 明确了空位缺陷浓度与HOR活性之间的构效关系。并从碱性HOR反应机理, CO分子与金属催化剂的轨道相互作用以及结构设计三个方面总结了高效和稳定的HOR催化剂的设计原则。目前, 由于界面环境的复杂性和缺乏原位技术, 催化剂表面上痕量中间体的光谱信息难以获得, 未来可在开发原位技术监测HOR过程中间体和催化剂的组分变化方面做出更多的努力, 以促进AEMFCs的商业化应用。

关键词: 氢氧化反应; CO耐受性; 磷空位; V_p-Pd₃P@C; 碗状半球

收稿日期: 2023-09-11. 接受日期: 2023-11-07. 上网时间: 2024-01-10.

*通讯联系人. 电子信箱: xlyang@gxnu.edu.cn (杨秀林), isimjant@sabic.com (Tayirjan Taylor Isimjan).

¹共同第一作者.

基金来源: 国家自然科学基金(52363028, 21965005); 广西自然科学基金(2021GXNSFAA076001); 大学生创新创业训练项目(202210602045); 广西研究生教育创新计划项目(YCSW2023140); 广西科技基地与人才课题(GUIKE AD20297039).